Military Technical College
Kobry El-Kobba,
Cairo, Egypt

11-th International Conference
on Aerospace Sciences &
Aviation Technology

A SUGGESTED NUMERICAL ALGORITHM FOR GEOMETRICALLY NONLINEAR AEROELASTIC BEHAVIOR

Mohammed Elhadi Ahmed Elsayed (PhD)*

ABSTRACT

A numerical simulation algorithm has been developed to investigate the effects of geometric nonlinearities on dynamic aeroelastic behavior of wing-like cantilever structures.

A geometrically nonlinear finite element formulation relevant to flexible structures has been adopted to model the structure using a degenerate-continuum shell element along with total Lagrangian formulation. Subsonic doublet lattice method (DLM) has been used to model the unsteady aerodynamics. To ensure full coupling between the structural and aerodynamic networks, infinite plate spline technique has been employed. This has facilitated the transfer of loads and displacements during the nonlinear analysis where the aerodynamic load is applied incrementally through a unique two-level time stepping procedure developed in the present work. The results obtained highlighted the effectiveness of the suggested numerical algorithm in capturing geometrically nonlinear behavior. Geometric nonlinearities showed additional nonlinear features that are not predicted by the linear approach.

KEY WORDS: Degenerate-continuum shells, geometric nonlinearity, unsteady aerodynamics, flutter and nonlinear aeroelasticity.

Nomenclature

B_{nl}	Displacement- strain matrix
D	Displacement vector
F	Aerodynamic force vector
H	Boolean matrix
K_t	Tangent stiffness matrix
k_r	Reduced frequency

* Assist. Prof., Karary Academy of Technology – Khartoum – Sudan, mohadi20@hotmail.com

INTRODUCTION

Nonlinear aeroelasticity had bubbled to the surface as a response to the continuous demand for faster airplanes and the consequent need to push the flight envelope further. When wings are very flexible, then wing flexibility coupled with relatively long span leads to the possibility of *large deflections* during normal flight operations [1]. These can no longer be analyzed solely within the standard linearized aeroelasticity theory; instead a nonlinear approach is preferable. Nonlinearities may introduce certain new types of phenomena which are not even indicated by the linear theory; limited amplitude oscillations were observed which could lead to long time fatigue failure [2].

As a consequence to the lack of effective nonlinear analytical models, research has turned toward the development of *integrated computational models* capable of capturing such possible interactions [3]. It had, thus, become necessary to re-examine and re-cast classical problems in the light of the possible effects of nonlinearities [2]. Unfortunately, computational approach models are faced with the fact that computational unsteady aerodynamics and computational structural dynamics are quite different. A *suitable interfacing technique* must be used. And the *time scales* are different [4].

In the context of nonlinear aeroelastic analysis, the previous efforts in the field either seem to lack a sufficiently power-full nonlinear structural models or/and are relatively complex and costly and most importantly are not amenable to preliminary design. These facts enhanced the demand to seek a simple and effective solution that is capable of performing nonlinear aeroelastic analyses.

STRUCTURAL MODEL

Element Choice

Classical shell theories are not useful for nonlinear, large displacement analysis of structures since the elements become distorted and the changes in the structural geometries cannot be accounted for accurately [5]. On the other hand, the degenerate shell element which does not resort to any shell theory is efficient, inherently general and simple compared to elements based on shell theories [6]. Degenerate shell element formulation accounts for full geometric nonlinearity, as they admit arbitrarily large displacements and rotations of the shell.

Incremental Deformation of a Continuum

A total Lagrangian formulation where all terms refer to the initial configuration has been adopted in the formulation in the nonlinear FEM model. The equilibrium is established using the principle of virtual work, which is expressed in terms of the well known energetically conjugate 2^{nd} Piola-Kirchhoff stress tensor and the Green-Lagrange strain tensor.

Nonlinear Finite Element Formulation

Element geometry

The basic element geometry is constructed using the co-ordinates of the middle surface nodes and the mid-surface nodal point normals, as in Figure (1), and is expressed in vector form as [7]:

$$r = \sum h_i(\xi,\eta)\bar{r}_i + \frac{1}{2}\sum h_i(\xi,\eta)a_i v_i \tag{1}$$

where h_i are the standard shape functions for a quadrilateral 8-node shell element. The unit vector v_i is defined by two parameters ψ_i and ω_i, as shown in Figure (2) where:

$$v_i^T = \{\cos\psi, \sin\psi\cos\omega, \sin\psi\sin\omega\}_i \tag{2}$$

This choice of rotation variables is due to Ramm [8] and was proven to perform well in geometrically nonlinear analyses. It accommodates for large rotation capability during the large deformation process and permits large rotations between successive load increments as it retains nonlinear nodal rotation functions (trigonometric) in the normal vector expression [9].

Displacement field

For any generic point of the degenerate shell elements, the displacement components, referred to the global co-ordinate system can be separated into the displacement of the shell mid-surface; and the relative displacement related to the rotations of the shell normal. The deflections follow as isoparametric:

$$d = \bar{d} + \Delta d = \sum h_i(\xi,\eta)\bar{d}_i + \frac{1}{2}\zeta\sum h_i a_i(v_i - v_{io}) \tag{3}$$

where v_{io} represents the initial unit vector in normal direction.

Green's strain

The compacted expression of the Green strain is given by

$$\mathrm{E} = \mathrm{E_l} + \mathrm{E_{nl}} = \left[\mathrm{H} + \frac{1}{2}\mathrm{A}(\theta)\right]\theta \tag{4}$$

where

$$H = \begin{bmatrix} 1 & 0 & 0 & 0 & 0 & 0 & 0 & 0 & 0 \\ 0 & 0 & 0 & 0 & 1 & 0 & 0 & 0 & 0 \\ 0 & 0 & 0 & 0 & 0 & 0 & 0 & 0 & 1 \\ 0 & 1 & 0 & 1 & 0 & 0 & 0 & 0 & 0 \\ 0 & 0 & 1 & 0 & 0 & 0 & 1 & 0 & 0 \\ 0 & 0 & 0 & 0 & 0 & 1 & 0 & 1 & 0 \end{bmatrix} \tag{5}$$

with A (θ) matrix form

$$A(\theta) = \begin{bmatrix} \frac{\partial u}{\partial x} & 0 & 0 & \frac{\partial v}{\partial x} & 0 & 0 & \frac{\partial w}{\partial x} & 0 & 0 \\ 0 & \frac{\partial u}{\partial y} & 0 & 0 & \frac{\partial v}{\partial y} & 0 & 0 & \frac{\partial w}{\partial y} & 0 \\ 0 & 0 & \frac{\partial u}{\partial z} & 0 & 0 & \frac{\partial v}{\partial z} & 0 & 0 & \frac{\partial w}{\partial z} \\ \frac{\partial u}{\partial y} & \frac{\partial u}{\partial x} & 0 & \frac{\partial v}{\partial y} & \frac{\partial v}{\partial x} & 0 & \frac{\partial w}{\partial y} & \frac{\partial w}{\partial x} & 0 \\ \frac{\partial u}{\partial z} & 0 & \frac{\partial u}{\partial x} & \frac{\partial v}{\partial z} & 0 & \frac{\partial v}{\partial x} & \frac{\partial w}{\partial z} & 0 & \frac{\partial w}{\partial x} \\ 0 & \frac{\partial u}{\partial z} & \frac{\partial u}{\partial y} & 0 & \frac{\partial v}{\partial z} & \frac{\partial v}{\partial y} & 0 & \frac{\partial w}{\partial z} & \frac{\partial w}{\partial y} \end{bmatrix} \tag{6}$$

where θ is the displacement gradient vector. The change in the displacement derivatives gradient (δθ) is related to the change in the nodal displacement derivatives (δp) as follows [7]

$$\delta\theta = \frac{1}{2} \begin{bmatrix} a_1^T & 0^T & 0^T & b_1^T & 0^T \\ a_2^T & 0^T & 0^T & b_2^T & 0^T \\ a_3^T & 0^T & 0^T & b_3^T & 0^T \\ 0^T & a_1^T & 0^T & c_1^T & e_1^T \\ 0^T & a_2^T & 0^T & c_2^T & e_2^T \\ 0^T & a_3^T & 0^T & c_3^T & e_3^T \\ 0^T & 0^T & a_1^T & d_1^T & f_1^T \\ 0^T & 0^T & a_2^T & d_2^T & f_2^T \\ 0^T & 0^T & a_3^T & d_3^T & f_3^T \end{bmatrix} \delta p = G\,\delta p \tag{7}$$

where

$$a_k = 2\left(J^{-1}(k,1)h_\xi + J^{-1}(k,2)h_\eta\right) \tag{8}$$

$$b_k = -D(a\sin\psi)z_k \tag{9}$$
$$z_k = \zeta h_\xi J^{-1}(k,1) + \zeta h_\eta J^{-1}(k,2) + hJ^{-1}(k,3)$$

$$\begin{aligned} c_k &= D(a\cos\psi\cos\omega)z_k \\ d_k &= D(a\cos\psi\sin\omega)z_k \\ e_k &= -D(a\sin\psi\sin\omega)z_k \\ f_k &= D(a\sin\psi\cos\omega)z_k \end{aligned} \tag{10}$$

D represents a diagonal matrix with diagonal terms between brackets.

Virtual work and internal force vector

The principle of virtual work has been employed to derive the equilibrium equations at any fixed time during the loading process. The virtual work (V) expression is defined as;

$$V = \int S^T \delta E_v dV_o - V_e \tag{11}$$

For small virtual displacements

$$\delta E_v = B_{nl}(p)\delta p \tag{12}$$

The first term contains the virtual work performed by the internal loads and V_e contains the virtual work performed by the external loads. Substitution from eq. (13) into the virtual work expression eq. (12) leads to;

$$V = \delta p_v^T \int B_{nl}^T(p) S dV_o - \delta p_v^T q_e = \delta p_v^T g \tag{13}$$

The term $\delta p_v^T g$ represents the incremental virtual work during a time interval Δt. The out-of-balance force vector, g, is thus obtained as

$$g = q_i - q_e = \int B_{nl}^T S dV_o - q_e \tag{14}$$

where for three-dimensional case the 2nd Piola- Kirchhoff stress, S, is given as

$$S^T = (S_{xx}, S_{yy}, S_{zz}, S_{xy}, S_{yz}, S_{xz}) = (S_{11}, S_{22}, S_{33}, S_{12}, S_{23}, S_{13}) \tag{15}$$

Stress and strain vector are to be substituted in a suitable constitutive relation.

Tangent stiffness matrix

The tangent stiffness matrix is derived by direct differentiation of the internal force vector in order to be fully consistent with the kinematic assumptions inherent in the model [7]. The final expression is given as

$$K_t = K_{t1} + K_{\sigma 1} + K_{\sigma 2} \tag{16}$$

where

$$\mathrm{K_{tl}} = \int \mathrm{B_{nl}^T D B_{nl} dV_o} = \int \mathrm{G^T [H + A(\theta)]^T D [H + A(\theta)] G dV_o} \tag{17}$$

with D being the constitutive matrix. The other contributions to K are given as [7]:

$$K_{\sigma 1} = \int G^T \hat{S} G dV_o \tag{18}$$

where

$$\hat{S} = \begin{bmatrix} \overline{S} & 0 & 0 \\ 0 & \overline{S} & 0 \\ 0 & 0 & \overline{S} \end{bmatrix}, \qquad \overline{S} = \begin{bmatrix} S_{11} & S_{12} & S_{13} \\ S_{21} & S_{22} & S_{23} \\ S_{13} & S_{23} & S_{33} \end{bmatrix} \tag{19}$$

and

$$K_{\sigma 2} \delta p = \iint \sum_{K=1}^{9} F(k) \delta G_k dV_o \tag{20}$$

where δG_k is the variation of the k_{th} component of matrix G and F (k) is the k_{th} component of the vector

$$F = [H + A(\theta)]^T S \tag{21}$$

System's Nonlinear Dynamic Equations

A Newmark's time integration scheme has been used to establish an algebraic system of pseudostatic equilibrium equations. The resulting nonlinear dynamic equations of motion are solved at each load step using modified Newton Raphson method. The general nonlinear dynamic equations of motion are as follows

$$Kd + M\ddot{d} + C\dot{d} - F = 0 \tag{22}$$

where M is the consistent mass matrix defined as in a standard FEM form [10].

developed by Harder and Desmarais [13] proved to be the most successful and has been adopted herein.

NUMERICAL IMPLEMENTATION

An Integrated System Routines for Aeroelastic Analysis (*ISRAA*) is a software system that integrates the essential disciplines required by time domain aeroelastic analysis. A unique two-stage time scale - as sketched in Figure (4) - has been used. Actually a local and a global time steps have been developed by the author. The local time stepping is related to the structure. The global time step is connected to the aerodynamics whereby the aerodynamic pressure is applied gradually.

Description of Input

A cantilevered rectangular wing-like structure is considered for this case. The geometry and material properties data are given in Table (1).

Table 1. Geometry and Material Properties of Cantilevered Rectangular Wing

Young's modulus (GPa)	69
Poisson's ratio	0.3
Shear modulus (GPa)	27
Density (kg/m^3)	2765
Thickness (m)	0.0127

Flight Conditions and Wing Discretization

An air density of $1.2247\ \ kg/m^3$ corresponding to sea level is used. The free stream Mach number is 0.50. A velocity list contains values from 150-225 m/s with 5 m/s increment per global time step and twenty reduced frequencies set from 0.8 to 0.0 has been used. The wing is divided into 7 chord-wise and 11 span-wise evenly cut divisions, which generate 6 by 10-aerodynamic boxes. Root and tip chord lengths are both 1.0089-m with a 2.0178-m semi-span length.

RESULTS AND DISCUSSION

oduction

The emphasis of the present work is on establishing the methodology and checking the vario ionality of the proposed numerical algorithm rather than presenting results for real *AIC's* as the latter need in one concern detailed structural and aerodynamic data of real form car

wings and in the other concern they need tedious and costly computer work which is not justified for such unreal cases.

Unsteady Aerodynamic Pressure Calculations

Figure (5) shows the variation of the real part of the unsteady aerodynamic pressure with dynamic pressure in the range of 0-14000 N/m². As the aerodynamics is jump started using a steady aerodynamic load, this jump-start is reflected as the jump at the beginning of the curve. This sudden jump declares the 'birth' of the unsteady aerodynamic load. However, at these low dynamic pressure values, the amplitudes of the unsteady aerodynamic pressure loads are infinitesimal. Between 13600 - 20000 N/m² dynamic pressures as shown in Figure (7) for the real part, low amplitude random oscillations commence with the mean of oscillation being continuously shifted towards lower values while divergent oscillations continue to grow. This is natural since as dynamic pressure increases, and so does the load, the wing deforms and different loaded equilibrium positions are reached.

Figure (9) gives the plot of the real part of the unsteady aerodynamic pressure force for the range of 20000-25000 N/m² dynamic pressure. Limited amplitude oscillations commence with more regular pattern, till at above 23500 N/m² dynamic pressures, motions tend to be more sinusoidal and divergent indicating approaching an instability boundary. However, as amplitudes of vibration increases geometric nonlinearity becomes increasingly important and in fact dominant.

In Figure (11) the real part of the unsteady aerodynamic pressure for the range of dynamic pressure between 25000 and 27500 N/m² is displayed. This range is characterized by a sinusoidal motion for the whole range. It exhibits an amplitude modulation whereby oscillations diverge and then converges for the dynamic pressure ranges of 25000 – 26000 N/m², then keeps nearly constant amplitude oscillations in the range between 26000- 27000 N/m². This reflects the instantaneous interaction between elastic and aerodynamic forces and may be attributed specifically to the gain of an additional stiffness due to the nonlinear formulation of the structure stiffness. The unsteady aerodynamic forces had dropped and could no longer pump the required amount of energy into the structure and thus the amplitude of oscillation and the total energy level out. However, beyond 27000 N/m² dynamic pressures divergent behavior with rapidly increasing amplitudes is observed.

Above a dynamic pressure of 27500 N/m² as shown in Figure (13) a pure sinusoidal behavior is observed with continuing divergent motion. From here and forward in time rapid increase in pressure amplitudes is observed. The divergent motion observed in these plots indicates that the restoring forces could no longer support the structure, and the unsteady aerodynamic pressures become dominant. At about 30700 N/m² dynamic

pressure, Figure (15), which corresponds to a flight speed of 224 m/s loss of convergence is observed and the program stops with singularity of the stiffness matrix indicating that the structure is not perfectly restrained now. However, the flutter or dynamic instability may be regarded as occurring at somewhat lower than 224 m/s speed.

Comparison between Linear and Nonlinear Cases

The unsteady aerodynamic pressures for both nonlinear and linear cases are demonstrated. At lower dynamic pressures (>0-14000 N/m²), unsteady pressure build-up trend is identical for both linear and nonlinear cases as shown in Figures (5) and (6). This may be attributed to the fact that at these lower values of dynamic pressure the aerodynamic loading –which builds-up with increasing dynamic pressure-, is small and has no contribution to the stiffness. However, the situation is quite different for higher than 14000 N/m² dynamic pressure as apparent from Figures (7) and (8). In these plots, the linear case curve serves as a mean of oscillation for the corresponding nonlinear case. The oscillatory response appearing in Figure (7) for the nonlinear case reflects the influence of nonlinear formulation. The used algorithm succeeded in capturing such infinitesimal changes, while the linear approach failed to predict such oscillatory motion. This points out the fact that geometrically nonlinear formulation becomes increasingly important as dynamic pressure, and hence the load, increases.

The linear solution displayed in Figure (10), however, shows a linear slow reduction in the unsteady aerodynamic force with increasing dynamic pressure which is also correct for the nonlinear case as can be observed from Figure (9). These amplitude oscillations only become divergent above a dynamic pressure of 23500 N/m². Inspecting Figures (11) and (12) for a higher range of dynamic pressure (25000- 27500 N/m²), almost identical observations can be concluded compared to the dynamic pressure range 20000-25000 N/m² shown in Figures (9) and (10).

At still higher dynamic pressure values, as shown by Figure (13) the real part of the unsteady aerodynamic pressure force for the nonlinear case continues to grow in a purely sinusoidal motion while gaining more and more energy indicated by the larger pressure amplitudes. The structure is extracting more energy from the free stream. This extra energy was known to induce more wing motions (elastic deformations) and thus causing continuous changes (increasing) in the unsteady aerodynamic loading till at a critical value of the dynamic pressure a dynamic instability occurs. Driving back to the linear solution and near a pressure of 28500 N/m² some fluctuating motion with sinusoidal type commences and further manifested for higher dynamic pressure values as shown in Figure (14) for the real part. An interesting observation here is that the curve oscillates about a continuously linearly decreasing mean of oscillation, and gradually at higher pressure values the curves start oscillating about a horizontal mean

under the influence of the elastic restoring forces and this is more obvious in Figures (16) for the real part where pure sinusoidal motion with divergent amplitudes is observed, and even at these high dynamic pressures the values of the unsteady aerodynamic pressures are very much smaller compared to those predicted by the nonlinear solution.

From the above, it is that the nonlinear formulation reveals a type of response which the linear solution fails to indicate and that the nonlinear formulation becomes increasingly important as dynamic pressure increases. Linear solution does overestimate the dynamic aeroelastic instabilities. This agrees with the well known fact that, unlike the predictions from linear analysis, in real situations it is possible for self-excited oscillations to develop even at speeds less than the flutter speed.

Wing Response Calculations

Time response curves give an idea about the behavior of the wing under the effect of unsteady aerodynamic loading and tell when a dynamic instability could occurs. A set of curves is shown that covers the whole range of dynamic pressure under consideration.

Figure (17) shows the time response curve of the structure for a dynamic pressure range between 0 - 14000 N/m². It is observed that a sudden rise in response occurs at the beginning of the curve due to the initial steady loading and it is this displacement that causes the sudden jump in the unsteady aerodynamic pressure as appearing in Figure (5). However, due to the dynamic equilibrium this does no longer continue and a constant equilibrium state is observed for the remaining of the dynamic pressure range. At about 13600 -N/m² dynamic pressure as shown in Figure (18) small random oscillatory motion with diverging amplitudes commences and continues as dynamic pressure increases. The mean of oscillation is gradually shifted towards lower values indicating a changing equilibrium state. However, random oscillations continue and cover the whole range of dynamic pressure between about 13600- 20000 N/m². This oscillatory motion is responsible for the type of unsteady aerodynamic pressure shown in Figure (7).

For the wing response shown in Figure (19) a pure oscillatory divergent motion for the whole range shown whereby the mean of oscillations is still fixed about the previous equilibrium position. This trend continues till at a value of 30700 N/m² dynamic pressure (Figure (20)) the stiffness of the structure could no longer supports the structure and the unsteady aerodynamic forces grow to much higher values that ultimately and naturally lead to structure failure.

Mid-wing Unsteady Pressure Calculations

An important feature of unsteady aerodynamic calculations is that due to the oscillatory nature, different locations in the wing are not necessarily in phase. This is apparent by comparing the process of building up of the unsteady aerodynamic pressures with increasing dynamic pressure for the wing-tip cases by that of mid-wing case shown in Figures (21), (22), (23) and (24) for real parts. Actually the character is similar but in the reverse order, i.e., as dynamic pressure increases, the unsteady aerodynamic pressure increases negatively for the real parts, till at the same value of dynamic pressure, i.e., about 14000 N/m², oscillatory motion commences with the mean of oscillation being continuously shifting indicating a changing equilibrium position under dynamic loading.

An interesting phenomenon observed in the dynamic pressure range between 25000-27500 N/m² as shown in Figures (11) and (23) is that the character is almost identical with the same amplitude modulation, i.e., the two points are in harmony. However, the two cases correspond to a sub-critical stage before the commencing of the divergent sinusoidal motion that grows rapidly and exponentially.

One observation, and indeed important, which is derived from plots for mid wing case-namely from Figure (24) is that wing tip goes unstable first. Also, after the critical dynamic pressure for the wing tip has passed, unsteady aerodynamic pressure amplitudes grows very rapidly within a small range of dynamic pressure and actually becomes many times higher than that at the wing tip at the moment when it had first gone unstable. This is a direct consequence of high and strong oscillatory unstable motion (high energy transfer) that commences after wing tip has gone unstable.

Mid-wing Response

Mid-wing response curves are given in Figures (25), (26), (27) and (28) for a pressure range from $0 < q < 31000$ N/m². After the jump-start ($q>0$), the wing response is constant at a fixed mean value for the whole dynamic pressure range (>0 – 14000 N/m²) shown in Figure (25).

However, at these lower dynamic pressure values it appears that the wing restoring forces balances the induced unsteady aerodynamic loads and a state of a 'static' equilibrium is attained, which very slowly shifts towards lower values indicating some effect of stiffening. This response is, however, typical in nature to that for the wing tip response shown in Figure (17) where tip deflection is higher. In the dynamic pressure range 14000 - 20000 N/m², as shown for the mid wing response, Figure (26), small random finite oscillations are observed with the mean of oscillations being very slowly shifted towards lower values. This response is, however, typical to that observed for the wing tip case shown in Figure (18) for the same dynamic pressure range. Same type of

response continues with highly and rapidly increasing oscillations that are getting sinusoidal for the dynamic pressure values up-to 31000 N/m² where failure occurs. This is evident from Figures (27) and (28). By comparing wing tip and mid-wing response during build up of dynamic loading, it is observed that both responses are almost identical with amplitudes of oscillation of mid wing being roughly an order of magnitude lesser than those observed at the wing tip.

Unsteady Aerodynamic Contour Plots

Contour plots give an idea about the unsteady aerodynamic pressure distribution over the wing surface at pre-selected dynamic pressures (time). The important features that can be observed from this set of results can be drawn as follows:

At low dynamic pressures as shown in Figure (29), unsteady pressures have small values with random distribution over the wing surface in accordance with wing response. Figures (30) and (31) display imaginary parts of unsteady pressures for both FE nodal points and aerodynamic control points at V= 150 m/s. As obvious from figures, contours almost reveal identical distributions for the unsteady aerodynamic pressure. This proves the effectiveness and correctness of the surface spline used. In fact this was the main motivation for drawing the contour plots, since one of the main sources of errors in aeroelastic analysis is in the interpolation between the structural and aerodynamic networks.

At much higher velocities, e.g. at a velocity of 224 m/s as shown in Figure (32) , the progressive built up of the unsteady aerodynamic pressure is clearly observed. Almost the whole of the wing is involved in this oscillatory motion, which spreads out with the magnitudes of the unsteady aerodynamic pressures growing exponentially. The wing is now involved in a dynamic instability, or rather flutter instability.

CONCLUSIONS AND RECOMMENDATIONS

Conclusions

The main problems that have been investigated include;

1. The geometrically nonlinear formulation along with the technique developed to apply the unsteady aerodynamic loads incrementally through the technique of *'local'* and *'global"* time stepping developed in this work has lead to an effective stiffness-updating scheme, which has proven to be very effective in capturing nonlinear behavior.
2. With such scheme inherent nonlinear effects have been explored and highlighted whereas the conventional linear solutions tested in this work failed to predict such types of behavior. The dynamic aeroelastic behavior predicted herein has proven to

agree with the well known mechanism with which dynamic aeroelastic instabilities usually occur; namely that, for small dynamic pressure values random oscillations are observed, where as the critical dynamic pressure had passed, oscillations become nearly sinusoidal with rapid amplitude growth on to the order of the plate thickness when the dynamic pressure is increased from 25% to 100 % beyond the value at which flutter had begun.

3. Full system simulation during the whole range of analysis has become possible. This is achieved through monitoring the process of build up of the unsteady aerodynamic pressures and wing motions up-to the point of instability if it does exist.

Recommendations for Future Work

1. Use of real wing configurations and/or with different plan-form parameters.
2. Establishing fatigue failure criteria from knowledge of stress amplitudes.
3. Aeroelastic tailoring using composite materials.
4. Inclusion of external disturbances and gust loads.
5. Higher order doublet lattice method needs to be implemented.
6. Further extension to include supersonic regime in the analysis.
7. Developing a criterion for optimizing the choice of time scales.

REFERENCES

1. Andruet, R. H., "Special 2-D and 3-D Geometrically Nonlinear Finite Elements for Analysis of Adhesively Bonded Joints", Ph. D. Thesis, Faculty of the Virginia Polytechnic Institute and State University, Blacksburg, Virginia, pp. 4-17, (1998).
2. Dowell, E. H., "Aeroelasticity of Plates and Shells", Noordhoff International Pub., Netherlands, pp. 1-48, (1975).
3. Cowan, T. J., Arena, Jr., A. S., and Gupta, K. K., "Development of a Discrete-Time Aerodynamic Model for CFD-Based Aeroelastic Analysis", AIAA-99-0765, (1999).
4. Kamakoti, R., Lian, Y., Regisford, S., Kurdila, S., and Shyy, W., "Computational Aeroelasticity using a Pressure-Based Solver", AIAA- 0869, (2002).
5. Liao, Chung-Li and Reddy, J. N., " Analysis of Anisotropic, Stiffened Composite Laminates using a Continuum-Based Shell Element", Computers and Structures, Vol. 34, No. 6, pp. 805-815, (1990).
6. Huang, H. C., "Static and Dynamic Analyses of Plates and Shells: Theory, Software and Applications", Springer- Verlag, pp 79-91, (1989).
7. Crisfield, M. A., "Nonlinear Finite Element Analysis of Solids and Structures- Vol. 1: Essentials", John Wiley and Sons, U.K., pp. 234-249, (1991) (*reprinted 2001*).
8. Hsiao, K. M., and Chen Y. R., "Nonlinear Analysis of Shell Structures by Degenerate Isoparametric Shell Element", Computers and Structures, Vol. 31, No. 3, pp.427-438, (1989).

9. Surana, K. S., "Geometrically Nonlinear Formulation for the Curved Shell Elements", International Journal for Numerical Methods in Engineering, Vol.9, pp. 581- 615, (1983).
10. Zienkiewicz, O. C., "The Finite Element Method", McGraw-HILL, UK, pp. 500-526, (1983).
11. Deb, A., and Booton, M., "Finite Element Models for Stiffened Plates under Transverse Loading", Computers and Structures, Vol. 28, No. 3, pp. 361-372, (1988).
12. Giesing, J. P., Kalman, T. P., and Rodden, W. P., "Subsonic Unsteady Aerodynamics for General Configurations: Direct Application of the Non-planar Doublet Lattice Method", AFFDL-TR-71-5, Part 1, Vol. 1, (1971).
13. Harder, R. L., and Desmarais, R. N., "Interpolation Using Surface Splines", AIAA Journal, Vol. 9, No. 2, pp. 189-191, (1972).

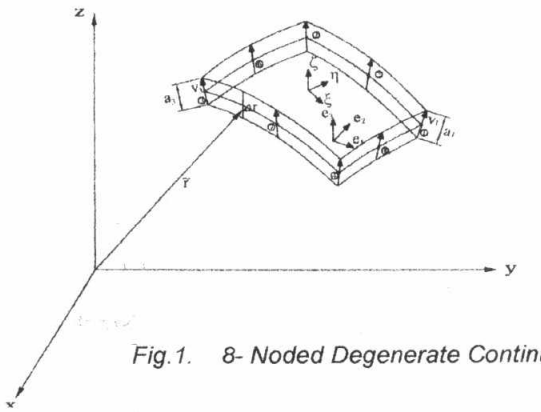

Fig.1. 8- Noded Degenerate Continuum Shell Element [7].

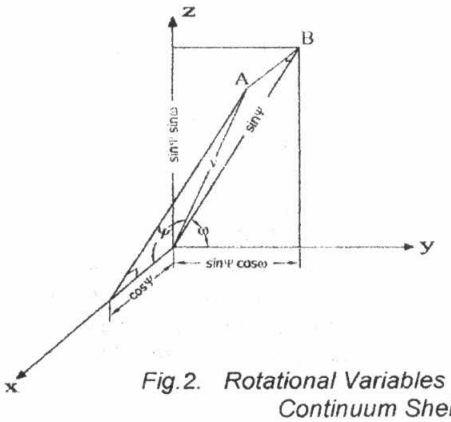

Fig.2. Rotational Variables Ψ and ω for Degenerate-Continuum Shell Element [7]

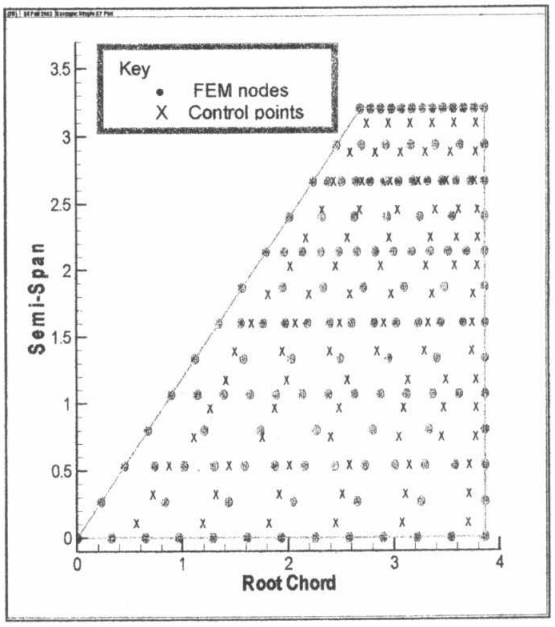

Fig.3. Schematic of Spline Plane

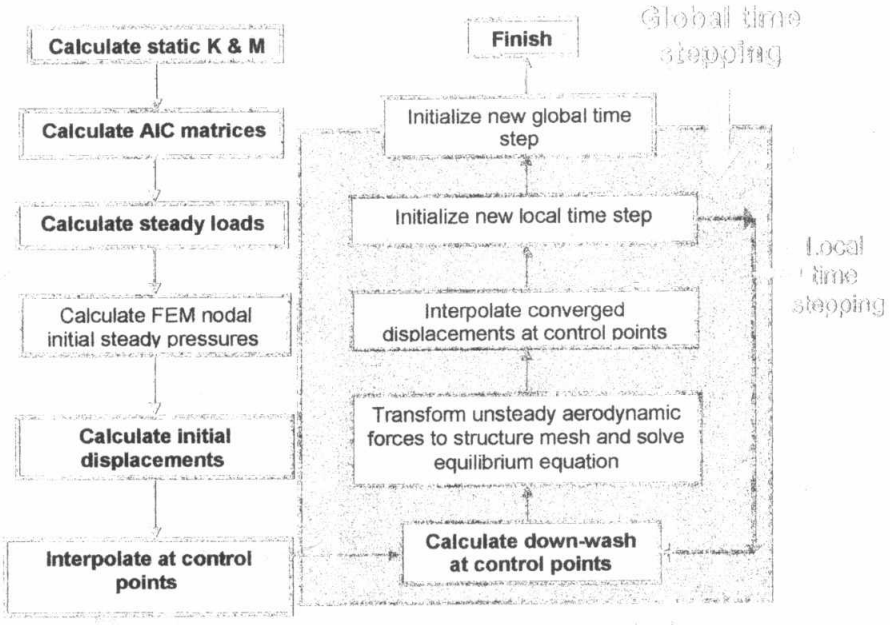

Fig.4. Block Diagram of Suggested Numerical Algorithm

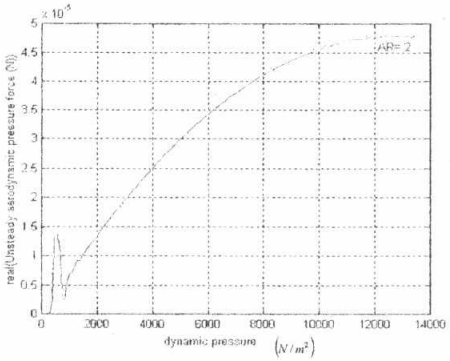

Fig.5. Real Part of
Unsteady Aerodynamic Pressure
(0 < q < 14000 N/m², Nonlinear case)

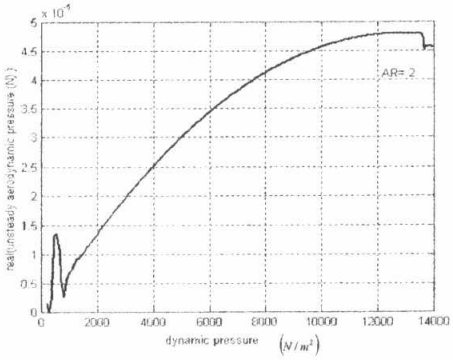

Fig.6. Real Part of
Unsteady Aerodynamic Pressure
(0 < q < 14000 N/m², Linear case)

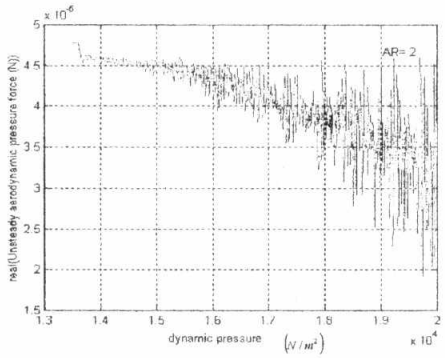

Fig.7. Real Part of
Unsteady Aerodynamic Pressure
(13000 < q < 20000 N/m², Nonlinear Case)

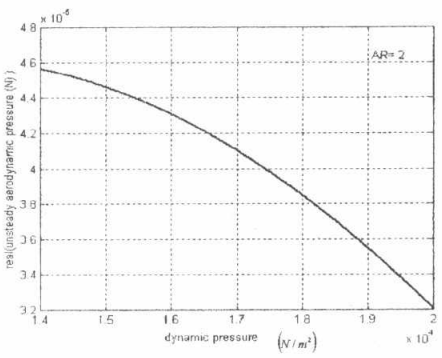

Fig.8. Real Part of
Unsteady Aerodynamic Pressure
(13000 < q < 20000 N/m², Linear case)

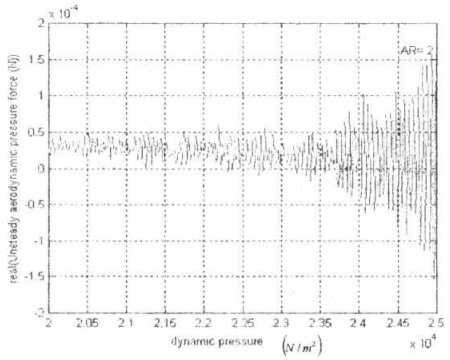

Fig.9. Real Part of
Unsteady Aerodynamic Pressure
(20000 < q < 25000 N/m², Nonlinear Case)

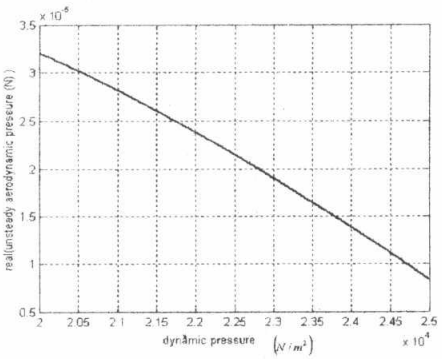

Fig.10. Real Part of
Unsteady Aerodynamic Pressure
(20000 < q < 25000 N/m², Linear Case)

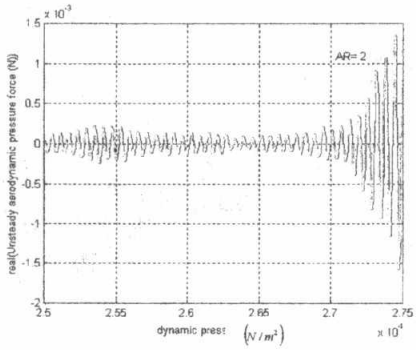

Fig.11. Real Part of
Unsteady Aerodynamic Pressure
(25000 < q < 27500 N/m², Nonlinear Case)

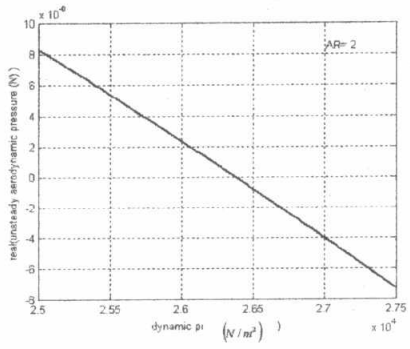

Fig.12. Real Part of
Unsteady Aerodynamic Pressure
(25000 < q < 27500 N/m², Linear Case)

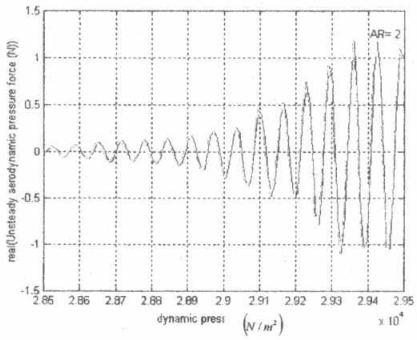

Fig.13. Real Part of
Unsteady Aerodynamic Pressure
(28500 < q < 29500 N/m², Nonlinear Case)

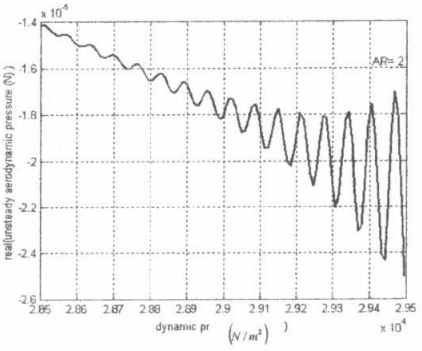

Fig.14. Real Part of
Unsteady Aerodynamic Pressure
(28500 < q < 29500 N/m², Linear Case)

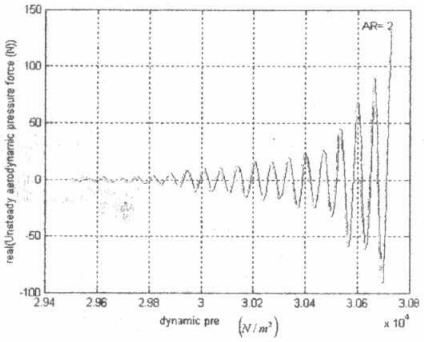

Fig.15. Real Part of
Unsteady Aerodynamic Pressure
(29400 < q < 30800 N/m², Nonlinear Case)

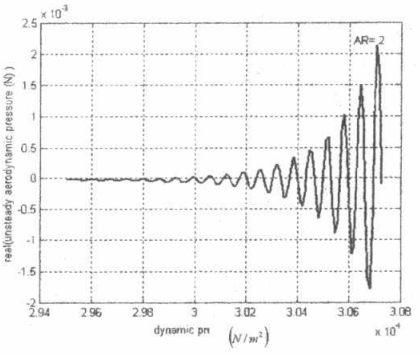

Fig.16. Real Part of
Unsteady Aerodynamic Pressure
(29400 < q < 30800 N/m², Linear Case)

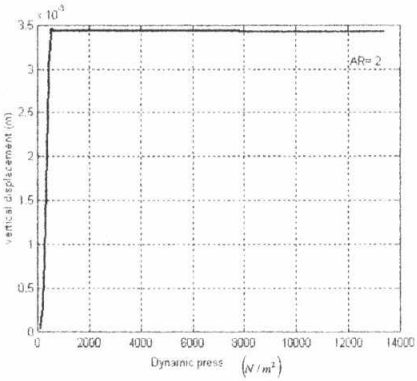

Fig.17. Wing-tip Response
(0 < q < 14000 N/m². Nonlinear Case)

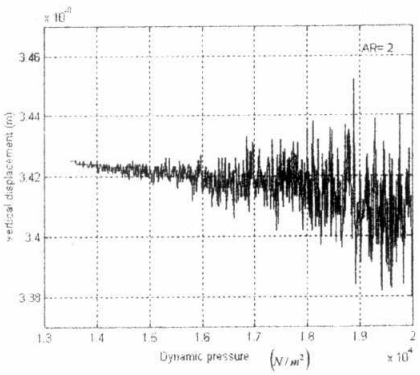

Fig.18. Wing-tip Response
(13000 < q < 20000 N/m², Nonlinear Case)

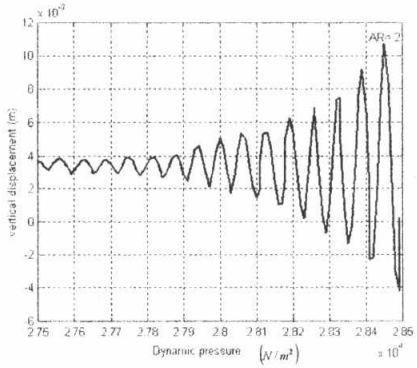

Fig.19. Wing-tip Response
(27500 < q < 28500 N/m², Nonlinear Case)

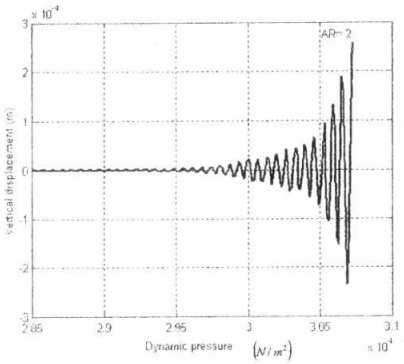

Fig.20. Wing-tip Response
(28500 < q < 31000 N/m², Nonlinear Case)

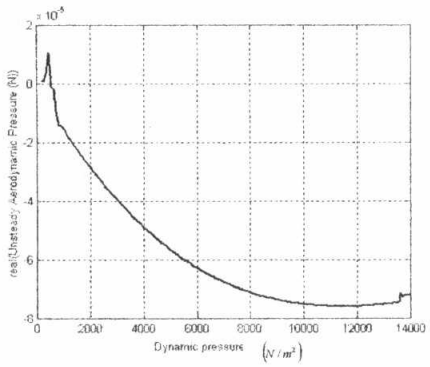

Fig.21. Real Part of
Unsteady Aerodynamic Pressure for Mid-wing
(0 < q < 14000 N/m², Nonlinear Case)

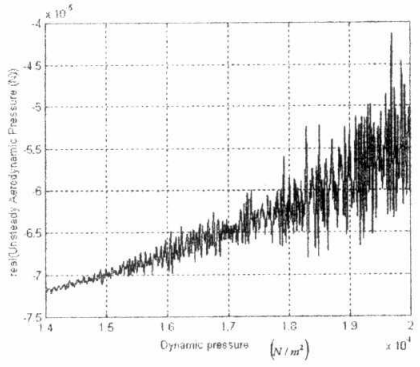

Fig.22. Real Part of
Unsteady Aerodynamic Pressure for Mid-wing
(14000 < q < 20000 N/m², Nonlinear Case)

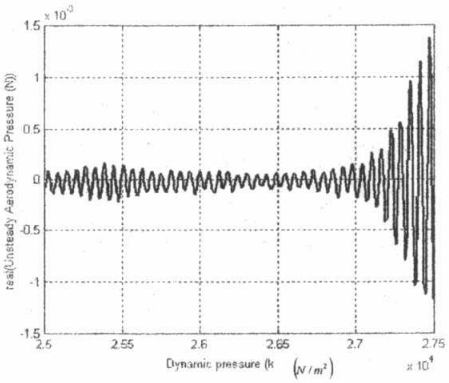

Fig.23. Real Part of
Unsteady Aerodynamic Pressure for Mid-wing
(25000 < q < 27500 N/m², Nonlinear Case)

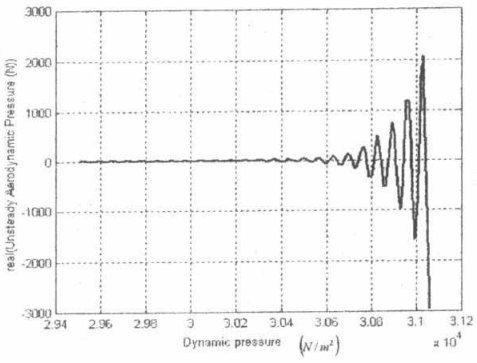

Fig.24. Real Part of
Unsteady Aerodynamic Pressure for Mid-wing
(29400 < q < 31200 N/m², Nonlinear Case)

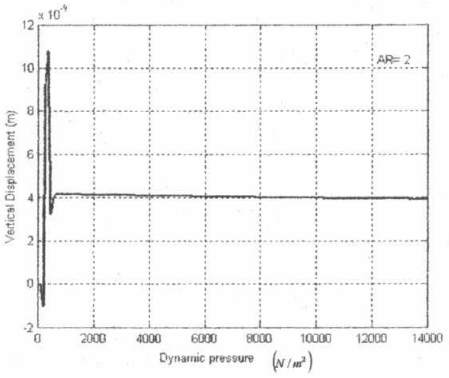

Fig.25. Mid-wing Response
(0 < q < 14000 N/m², Nonlinear Case)

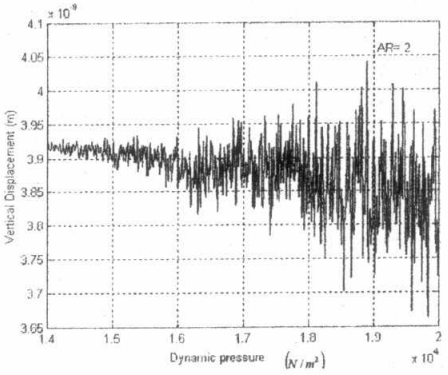

Fig.26. Mid-wing Response
(14000 < q < 20000 N/m², Nonlinear Case)

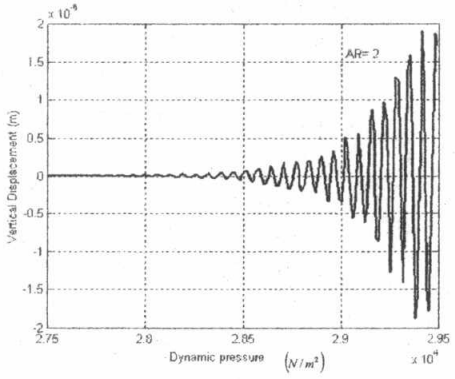

Fig.27. Mid-wing Response
(27500 < q < 29500 N/m², Nonlinear Case)

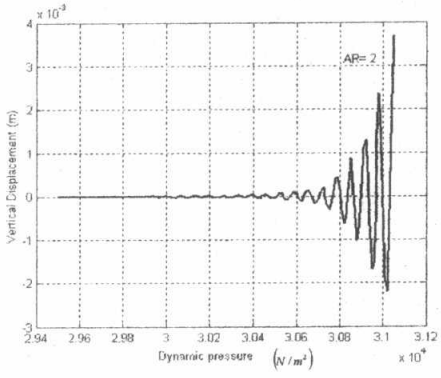

Fig.28. Mid-wing Response
(29400 < q < 31200 N/m², Nonlinear Case)

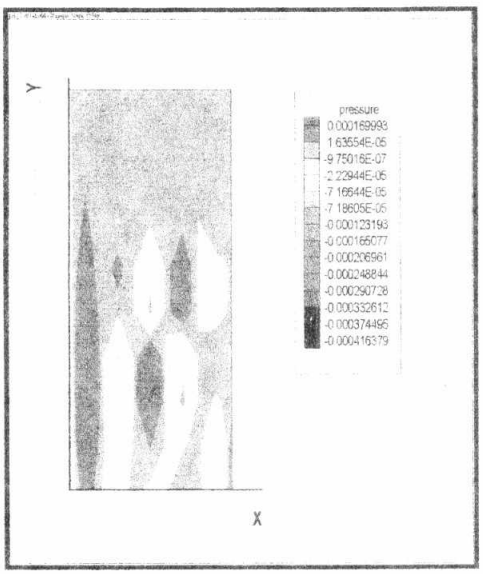

Fig.29. Contour Plot for Real Part of Unsteady Aerodynamic Pressure Interpolated at FEM Nodal Points (V= 150 m/s)

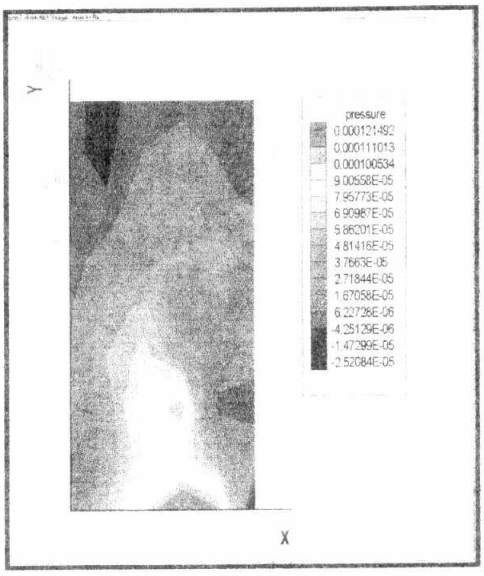

Fig.30. Contour Plot for Imaginary Part of Unsteady Aerodynamic Pressure Interpolated at FEM Nodal Points (V= 150 m/s)

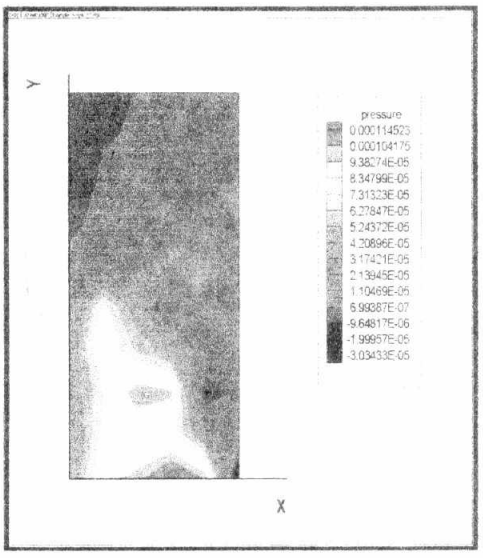

Fig.31. Contour Plot for Imaginary Part of Unsteady Aerodynamic Pressure at Aerodynamic Control Points (V= 150 m/s)

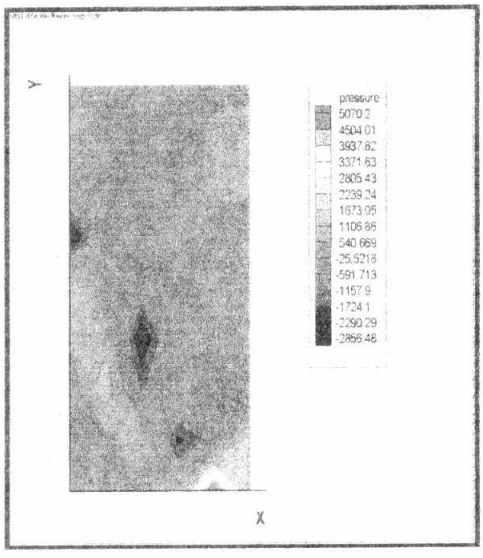

Fig.32. Contour Plot for Real Part of Unsteady Aerodynamic Pressure Interpolated at FEM Nodal Points (V=224 m/s)